

Article

Analysis of Flow Past a Double-Slanted Ahmed Body

Matthew Aultman * and Lian Duan 

Mechanical and Aerospace Engineering Department, The Ohio State University, Columbus, OH 43210, USA; duan.322@osu.edu

* Correspondence: aultman.4@osu.edu

Abstract: For this study, Improved Delayed Detached-Eddy Simulations (IDDES) were used to analyze the wake of a modified Ahmed body with varying upper and lower slants. The modified geometry produced a constant projected vertical base area, ensuring that the base and slant drag were a function of the pressure caused by the wake structures. Except at extreme slant angles, the general structures of the wake were a base torus with two pairs of streamwise-oriented vortices on each slant. These structures strongly correlated with the drag contribution of the rear surfaces: the torus with the vertical base and the streamwise-oriented vortices with the slants. As such, the base drag was minimized when the torus was most centrally aligned with the base, producing the largest stagnation region. Two slant-drag minima developed corresponding to two regimes of vortical flow on opposing slants. On one slant, the vortices were attached, and the drag correlated with the size and strength of the vortices. On the other slant, the vortices separated, and the drag correlated with the slant normal due to a more uniform pressure. This demonstrates a rich and complex set of interactions that must be managed in the development of base drag caused by wake flows.

Keywords: wake flow; bluff body flow; three-dimensional wake structures; vortex flows; base drag



Academic Editor: Mesbah Uddin

Received: 23 December 2024

Revised: 23 January 2025

Accepted: 29 January 2025

Published: 31 January 2025

Citation: Aultman, M.; Duan, L. Analysis of Flow Past a Double-Slanted Ahmed Body. *Fluids* **2025**, *10*, 35. <https://doi.org/10.3390/fluids10020035>

Copyright: © 2025 by the authors. Licensee MDPI, Basel, Switzerland. This article is an open access article distributed under the terms and conditions of the Creative Commons Attribution (CC BY) license (<https://creativecommons.org/licenses/by/4.0/>).

1. Introduction

Base pressure drag can contribute up to 50% of the total force on automotive vehicles caused by the highly separated base wake [1,2]. These base wakes are extremely complex, consisting of regions of separation, reattachment, recirculation, multiple merging shear layers, and vortices. Massive changes in these structures can occur due to only minor changes in vehicle geometry, leading to large changes in vehicle drag [3,4]. Due to the high complexity of base wakes and their sensitivity to small changes in geometry, it has been extremely difficult to characterize base wakes in a way that directly connects them to the subsequent base drag. By developing a clear and simple connection between the wake structure and the base drag, engineers can design flow control methods to produce a specific wake structure that is favorable for their design goals.

A great deal of work has been conducted over the years to characterize bluff body wakes and analyze their impact on base drag. In the seminal work of Ahmed et al. [3], the drag on the Ahmed body was found to increase with the rear slant angle for angles above 10° until a critical angle of 30°, at which point a drag crisis developed, resulting in a change in the wake flow. Before the drag crisis, streamwise-oriented vortices developed on the slant, producing a low-pressure footprint [3,5]. Both the size and pressure deficit of the low-pressure footprint were found to be related to the strength of the streamwise-oriented vortices [6]. Thus, reducing the strength of the vortices has proven beneficial in

reducing drag [7–10]. Above the critical angle, the pressure becomes relatively uniform as the flow completely separates and the vortices are no longer present [3,5,11]. Eliminating the vortices causes a drag reduction, which has led many to develop flow control methods to take advantage of the phenomenon [7–10,12,13]. While eliminating the vortices reduces drag, some flow control devices lose effectiveness with a different wake structure [14].

Although the rear slant is a major contributor to the total drag, the vertical base also produces a substantial proportion of the total vehicle drag for the Ahmed body [3]. Various studies have noted that the drag is connected to the wake length. However, there are discrepancies, as some studies have observed a decrease in drag with increasing wake length [7,15,16], while others have observed an increase in drag with increasing wake length [17]. This suggests that there may be a change in the wake structure that may not correlate directly with the wake length. Although the streamwise vortices have been heavily characterized in their general structure, the wake structure past the vertical base has had substantially less focus.

Despite the clear and definitive characterization of the base wake structure, additional flow control studies have targeted drag reduction on the base through the implementation of a lower slant (i.e., diffuser) [18–21]. These devices add further complexity to the wake structure, as with the rear slant on the upper body, a basic diffuser can introduce both streamwise-oriented vortices and separated flows [18–21]. Although streamwise-oriented vortices produce a higher drag prior to the drag crisis for the upper slant, there is actually a decrease in drag that develops in this regime for a diffuser [18,19]. This reversal in trends between the upper-body slant and the lower-body diffuser does not carry over when separation occurs, as separated flows in the diffuser can still lead to a drag reduction [20,21]. This change raises questions about the complex interaction between the vortices forming on the upper and lower slants and the structures past the vertical base, as well as their individual contributions to the total drag.

The individual surface contributions to the total drag have been a challenge since the original work by Ahmed et al. [3]. The authors observed that with increasing slant angle, the drag contribution of the vertical base tended to decrease. However, the exact relationship between the wake and the slant angle is hard to determine since the base continually shrinks with increasing slant angle, effectively sharpening the body. Sharpening a bluff body or streamlining the geometry, sometimes referred to as boat-tailing, is well known to decrease drag [22]. This varying area makes it difficult to connect the individual drag contributions of the slant and the base to the total drag, especially when connecting the effects of the individual wake structures, let alone adding further wake complexity with a diffuser.

Thus, the goal of this work is to better understand the complex three-dimensional (3D) wake structures behind a generic bluff body and their interaction with the vehicle body to produce drag. To achieve this goal, we developed a modified Ahmed body with varying upper and lower slants to produce a complex wake with multiple interacting structures, but with a constant projected vertical base area (Section 2.1). A constant base area facilitates the characterization of the individual drag contributions of the wake structures to the slants and the base. Computational Fluid Dynamics (CFD) simulations based on Improved Delayed Detached-Eddy Simulations (IDDES) were performed to capture the entire wake flow. To provide confidence in the solution, multiple meshes were tested (Section 2.2) in the IDDES setup (Section 2.3) to confirm grid convergence, and the simulations were further validated with experiments (Section 2.4). The drag was then determined for multiple slant angles and subsequently broken down into contributions from the different components of the vehicle base, before being connected to structures within the wake (Section 3). All findings are summarized in Section 4.

2. Simulation Details

2.1. Geometry

In the current study, we utilized the full-scale Ahmed body [3] with length $L = 1.044$ m, height $H = 0.389$ m (excluding pins), and width $W = 0.288$ m, given that it is a heavily simplified geometry and a staple in studies of automotive aerodynamics. We initially used the standard Ahmed body with a fixed slant angle as a baseline configuration. The base height h was then fixed to ensure both a constant base area and a constant projected slant area, regardless of upsweep and downsweep. In order to accommodate both an upsweep angle (β) and a downsweep angle (α), the Ahmed body was modified to have a fixed streamwise slant location (Figure 1). The slant location was selected to align with the streamwise location of the baseline Ahmed body. As a baseline, we chose a slant of 40° . This ensured that there was a fully separated wake for both extremes of the downsweep and upsweep angles, i.e., $\alpha = 40^\circ$ and $\beta = 40^\circ$, respectively [20,21]. With the fixed base height h and streamwise location of the two slants, the upsweep angle β then became a function of the downsweep angle α . Thus, the entire geometry could be modified via α . The different upsweep and downsweep angles analyzed in this work are listed in Table 1.

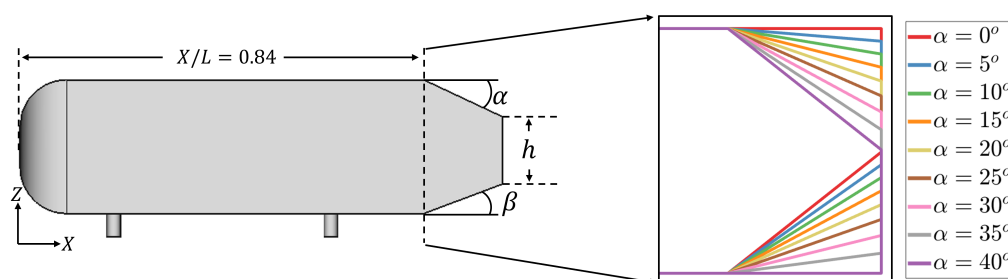


Figure 1. Geometry of double-slanted Ahmed body, including both upsweep and downsweep surfaces with fixed base height h . Different base geometry profiles are shown as a function of the downsweep angle α .

Table 1. Variations in the double-slanted Ahmed body’s upsweep and downsweep angles for this study.

Downsweep α (Degrees)	Upsweep β (Degrees)
40.0	0.0
35.0	7.9
30.0	14.7
25.0	20.4
20.0	25.4
15.0	29.7
10.0	33.5
5.0	36.9
0.0	40.0

2.2. Meshes

The meshes were constructed using OpenFOAM’s built-in blockMesh and snappy-HexMesh for the background and full meshes, respectively. The initial background mesh was a uniform Cartesian grid with a spacing of $\delta = 0.125$ m. General refinement regions were then added using three boxes surrounding the vehicle model (listed as large, medium, and small boxes) and an additional refinement box to better resolve the base (base refinement box) (Figure 2). Additional refinements were added to the ground (ground refinement) and around the vehicle surface extending 0.02 m from the body (body refinement) to better resolve the boundary layers on the ground and the vehicle body. Further

boundary layer refinement was added through inflation layers. Each of the ground and vehicle body surfaces was given inflation layers of 25 and 10 layers, respectively (Figure 3). This ensured that the majority of the surface had a $y^+ < 10$ for both the body and the ground. On the body in particular, 96% of the cells had a $y^+ < 10$, with an average of $y^+ \sim 4$. A similar distribution of y^+ was found to be effective for wall-modeled LES in automotive geometries [23]. The maximum values for both the body and ground (within the region of ground refinement) occurred at the junction of the mounting pins, where the inflation layers distorted to accommodate the surface discontinuity. While this ultimately resulted in a wall-modeled grid, the effects of wall-modeling on automotive flow fields are believed to be low compared to a wall-resolved grid, according to recent results reported in the Second Automotive CFD Prediction Workshop [24]. The refinement regions were then adjusted to various grid spacings to create two different meshes. More details on the meshes can be found in Table 2.

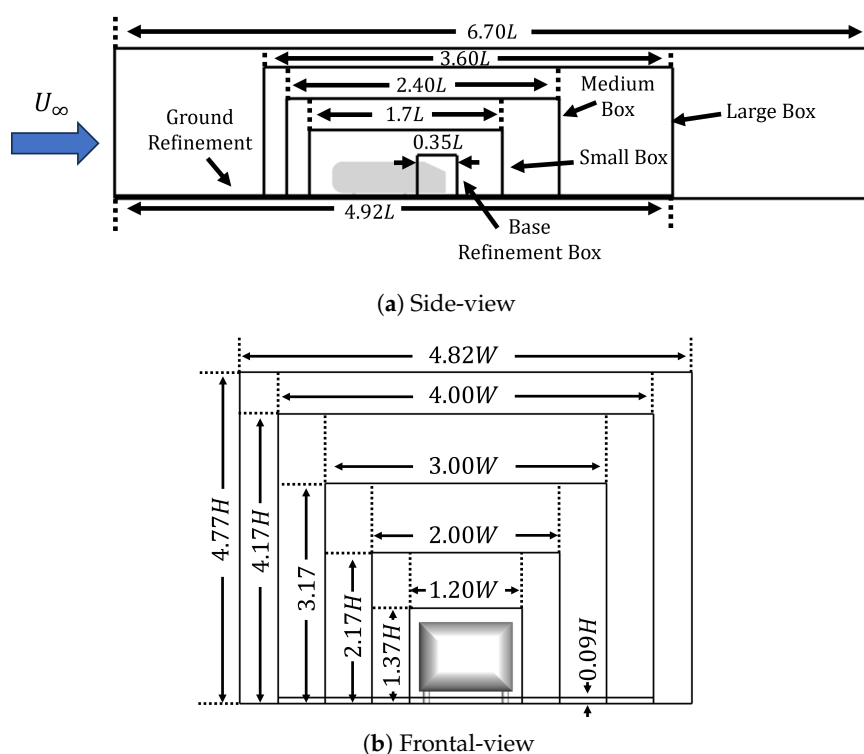


Figure 2. Refinement boxes used to define meshes.

Table 2. Mesh refinement regions for the 25° Ahmed body case.

	Mesh 1	Mesh 2
Base Mesh Size (m)	0.125	0.125
Ground Refinement (m)	0.008	0.008
Body Refinement (m)	0.002	0.002
Base Refinement Box (m)	0.004	0.002
Small Box (m)	0.008	0.004
Medium Box (m)	0.016	0.008
Large Box (m)	0.031	0.016
y^+ minimum (body)	0.06	0.06
y^+ maximum (body)	137.58	142.39
y^+ average (body)	~ 4	~ 4
y^+ minimum (ground)	0.08	0.05
y^+ maximum (ground)	341.10	252.42
Total cells (millions)	14.9	35.2

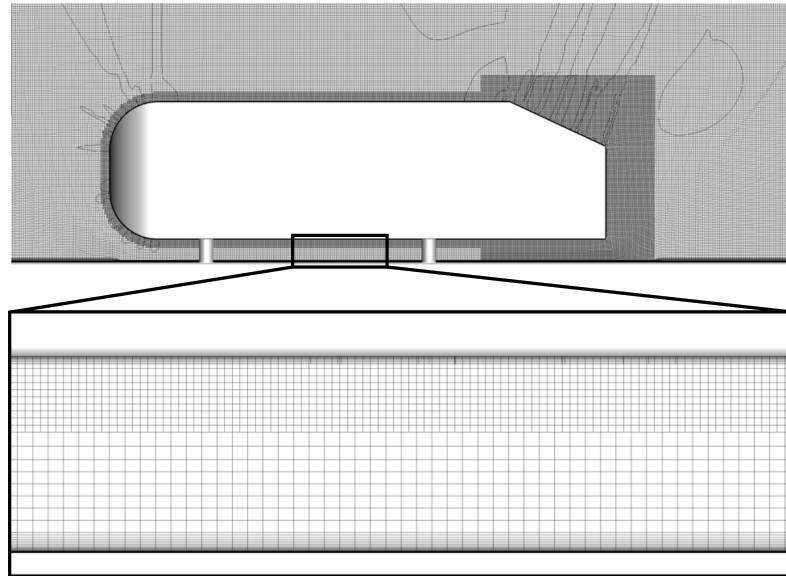


Figure 3. Slice of Mesh 2 along the centerline $y = 0$ for the 25° Ahmed body, with the inset showing the inflation layers on the ground and vehicle body.

2.3. Numerical Setup

The model was placed in a hexahedral box with dimensions of $7 \text{ m} \times 1.875 \text{ m} \times 1.375 \text{ m}$ in the streamwise, spanwise, and road-normal directions, respectively. The spanwise and road-normal dimensions were selected to roughly align with the nozzle dimensions of the experiments in Lienhart and Becker [25] while allowing for a uniform background grid spacing of 0.125 m . For the boundary conditions, a uniform velocity inlet of 40 m/s was used at the upstream end of the domain. The distance between the vehicle nose and the inflow plane was adjusted iteratively to match the experimental upstream profile in Lienhart and Becker [25], with the final distance being 2 m . At the downstream end, a pressure outlet was set. The sides and top of the domain were set to a symmetry condition to model the effects of the free shear layer from the $3/4$ open jet without having to resolve the shear layer. The vehicle body and ground were set to a no-slip wall condition.

We utilized OpenFOAM (v1912) to run Improved Delayed Detached-Eddy Simulations (IDDES) [26]. IDDES have the advantage of blending Large-Eddy Simulations (LES) and Detached-Eddy Simulations (DES) in a way that acts as a wall-modeled LES with sufficient grid refinement. This method has been found to be accurate in automotive applications at a reduced cost compared to LES [27]. Moreover, unsteady simulations of this nature have performed well in predicting incremental changes in complex wake flows [28]. The IDDES were solved using OpenFOAM's pimpleFoam solver, which combines the SIMPLE [29] and PISO [30] algorithms. For the fluxes, a second-order linear scheme was applied, with upwinding used only for inviscid fluxes. Time-marching used a second-order backward scheme with a time-step size of $\Delta t U_\infty / L = 3.8 \times 10^{-3}$ ($1 \times 10^{-4} \text{ s}$) corresponding to an average local Courant number of $Co = \Delta t |\bar{u}| / \sqrt[3]{Vol} = 1$, where U_∞ is the free stream velocity, $|\bar{u}|$ is the magnitude of the local time-averaged cell velocity predicted by an initial Reynolds-Averaged Navier–Stokes (RANS) solution, and Vol is the local cell volume. This method has been found to be effective in reducing the computational cost of unsteady simulations while still producing accurate time-averaged flow fields [31]. Two corrective steps were used for pimpleFoam, while two sub-iterations were used for each time step. The simulations were run out for a total of 20 convective times tU_∞ / L (0.522 s) after a washout of 5 convective times (0.1305 s). This was found to be sufficient to ensure that the time-averaged drag coefficient $\overline{C_D}$ ($\overline{C_D} = \overline{D} / [q_\infty A]$, where \overline{D} is the time-averaged drag, q_∞ is the freestream dynamic pressure, and A is the frontal area) changed by less than

one count ($\Delta \overline{C_D} = 0.001$ is one count) over the last 5 convective times (Figure 4) and that the time-averaged streamwise velocity profiles \bar{u} along the vehicle centerline converged (Figure 5).

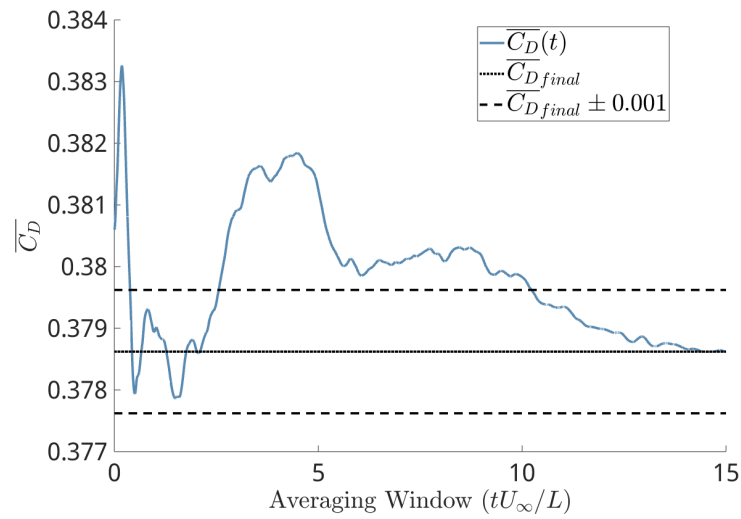
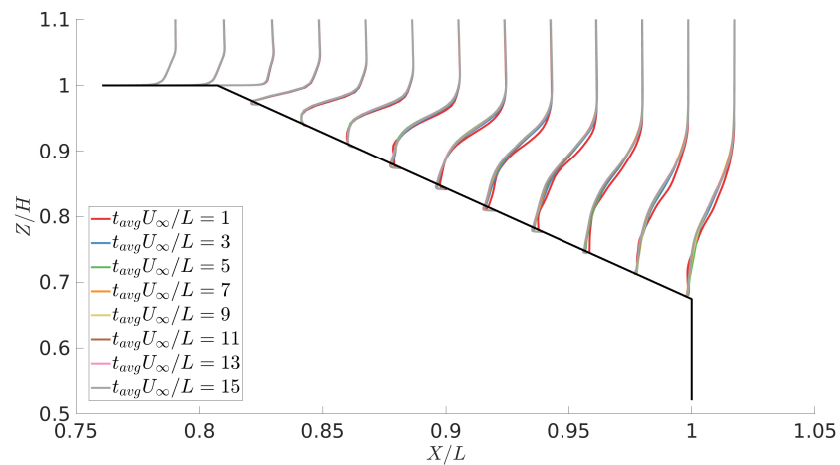
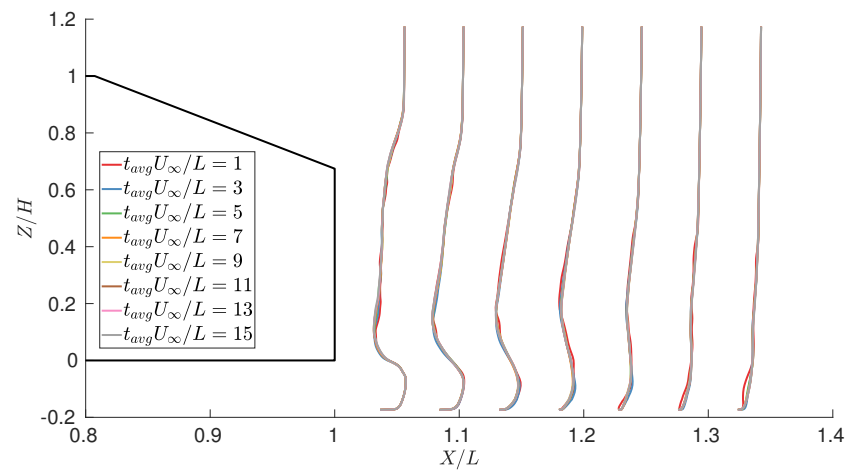


Figure 4. Convergence of the time-averaged drag coefficient $\overline{C_D}$ as a function of time.



(a) Slant Boundary Layer Profiles



(b) Wake Profiles

Figure 5. Comparison of the time-averaged (a) slant boundary layer and (b) wake streamwise velocity profiles \bar{u}/U_∞ between different averaging windows $t_{avg}U_\infty/L$ along the vehicle centerline ($y = 0$) for the 25° Ahmed body case.

2.4. Grid Convergence and Comparison with Experiments

In order to ensure that our numerical setup was accurate, we initially simulated flow around the 25° Ahmed body to compare with an existing dataset from Lienhart and Becker [25], which has been made publicly available [32]. Figure 6 shows a comparison of the time-averaged streamwise velocity profiles \bar{u} predicted by the IDDES with those of the experiments along the vehicle centerline ($y = 0$). Upstream of the vehicle, the 2 m distance between the inlet and vehicle nose was sufficient to ensure a quality match in the velocity profile 0.4 m upstream of the vehicle (Figure 6a). Along the body, upstream of the slant (Figure 6b), there was excellent agreement between the experiments and the simulations. However, once downstream of the roof/slant junction, there was a slight overprediction of separation from the simulations, and increasing the mesh resolution hardly improved the comparison. Although not shown, switching the turbulence model to Delayed Detached-Eddy Simulations (DDES) resulted in comparisons that were nearly identical to those of IDDES. Similar errors were found by Ashton et al. [33], who also reported that the IDDES results for the Ahmed body did not change with different turbulence models, wall models, or solvers. When examining the vehicle wake (Figure 6c), the difference between the experiments and simulations was even more marginal, indicating that this error produced only slight differences from the experiments. Thus, the current setup is considered sufficient to produce accurate results in the wake. The results presented in the rest of this paper utilize the finer mesh, given the slight differences observed.

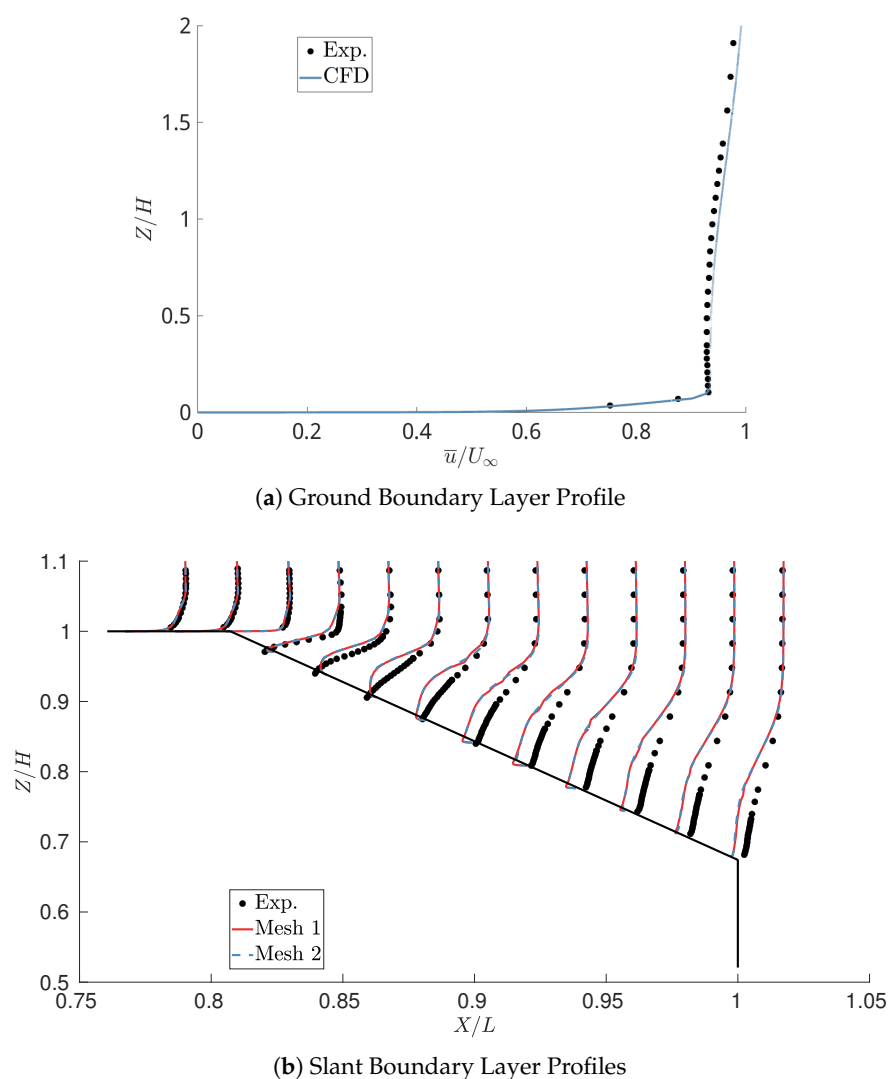


Figure 6. Cont.

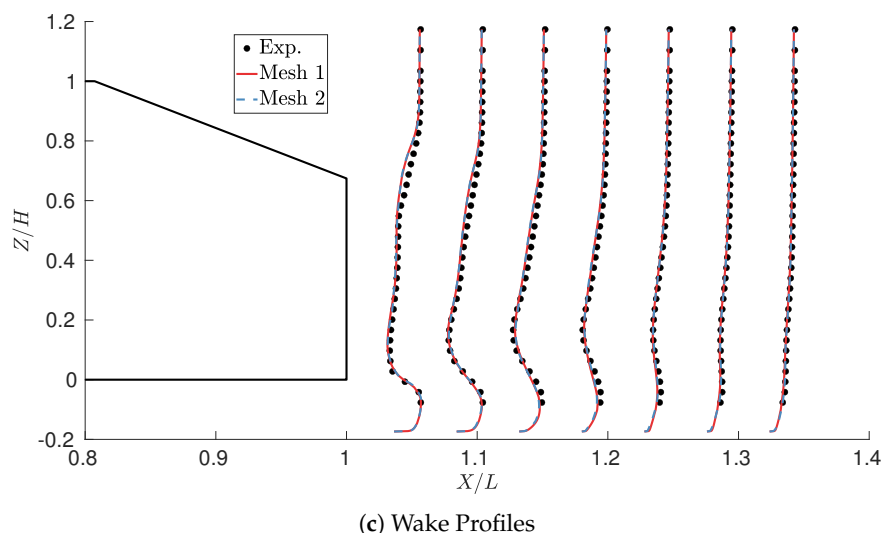


Figure 6. Comparison of the time-averaged (a) ground boundary layer at 0.4 m upstream of the model nose, (b) slant boundary layer, and (c) wake streamwise velocity profiles (\bar{u}/U_∞) between CFD and experiments [25] along the vehicle centerline ($y = 0$) for the 25° Ahmed body case.

3. Results and Discussion

To begin our analysis, Table 3 shows the time-averaged lift and drag coefficients $\overline{C_L}$ and $\overline{C_D}$, respectively, as a function of the upper slant angle (downsweep angle) α , where the force coefficient $\overline{C_F} = \overline{F}/(q_\infty A)$. The lift produced by the vehicle was a strong function of α , fluctuating between positive lift and extremely negative lift (positive downforce) for $0^\circ \leq \alpha \leq 40^\circ$. The net lift variation was more than 600 counts ($\Delta C_F = 0.001$ is 1 count), ranging from -0.5319 to 0.0829 . Similar variations in C_L have been found for the Ahmed body when only the upper slant angle was changed [19,34,35]. On the other hand, drag was substantially less sensitive to the upper slant angle than lift, with a variation of only 35 counts over $0^\circ \leq \alpha \leq 40^\circ$.

Table 3. Time-averaged force coefficients as a function of the upper slant angle α .

α	$\overline{C_L}$	$\overline{C_D}$
0	-0.2624	0.2620
5	-0.1242	0.2333
10	-0.0779	0.2267
15	0.0057	0.2313
20	0.0829	0.2323
25	-0.1694	0.2446
30	-0.5319	0.2597
35	-0.3106	0.2382
40	0.0020	0.2476

Figure 7 further shows the drag trends with respect to the upper slant angle α . Like the single-slanted Ahmed body, the drag of the double-slanted Ahmed body exhibited a parabolic variation with α , producing a clear minimum at $\alpha = 10^\circ$. Increasing the angle beyond 10° led to an increase in drag until $\alpha = 30^\circ$, when a sudden decrease in drag occurred. For the single-slanted Ahmed body, previous studies have found that the flow behind the base transitions from the vortex regime into the wake regime at $\alpha = 30^\circ$. The wake regime is characterized by fully separated flow over the rear slant, which leads to minor changes in drag up to at least $\alpha = 40^\circ$. However, for the double-slanted Ahmed body, the drag increased by up to 10 counts from the local minima from $\alpha = 35^\circ$ to 40° .

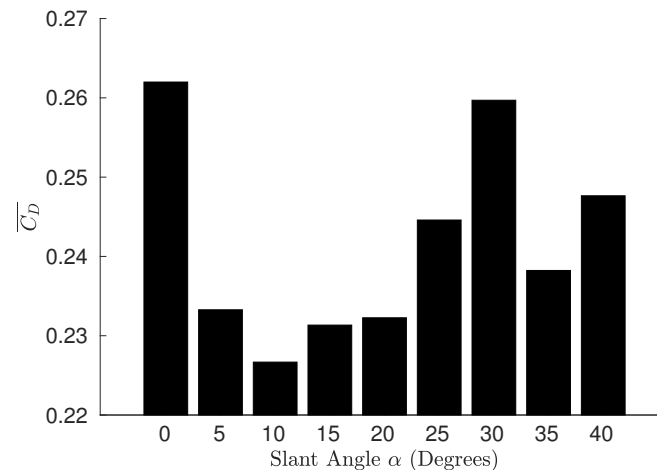


Figure 7. Time-averaged total vehicle drag coefficient $\overline{C_D}$ with respect to the upper slant angle α .

Figure 8 shows the contribution of the total drag between the different rear surfaces $\overline{C_{D_i}}$ (i indicates the contribution to the total drag coefficient of the surface(s)) to further illustrate the complex interactions between these different surfaces. The drag contribution of the base was consistently lower than that of the two slants. Although lower, the variation in the base drag over the different slant angles was actually larger than that of the slant drag coefficient ($\Delta\overline{C_{D_i}} = 31$ counts versus 28 counts, respectively). Additionally, there was a minimum in the base drag at $\alpha = 20^\circ$. However, this slant angle did not result in minimal total drag. Rather, due to the larger contribution of the slants to the total drag, the two minima in slant drag at $\alpha = 10^\circ$ and 35° aligned with those in total drag. Breaking down the slant drag between the upper and lower slants showed that the minima in slant drag occurred when one of the two slants dominated the slant contribution to the drag. When the contributions from the two slants were nearly equal ($\alpha = 20^\circ - 30^\circ$), the slant drag was at its peak.

To further elucidate the development of drag on the different surfaces, Figure 9 visualizes the pressure distribution on the base and the slants through the surface pressure coefficient $C_p \equiv \overline{P}/q_\infty$, where \overline{P} is the time-averaged static pressure. Focusing first on the vertical base, we observed high pressure near the center associated with the rear stagnation point of the wake highlighted by a contour line of $C_p = -0.09$. At the extreme angles of $\alpha = 0^\circ$ and 40° , a clear low-pressure footprint formed near the outer span of the base. At $\alpha = 20^\circ$, where the downsweep and upsweep angles had similar values (Table 1), the stagnation region increased in size with larger pressure values, while the outboard low-pressure footprint disappeared, resulting in minimum base drag. Interestingly, this occurred when $\alpha = 20^\circ$ rather than 25° , where the pressure distribution was nearly symmetric on a road-normal (Z) plane. Moving on to the slants, at higher angles, the pressure distribution across the slant was relatively uniform, aligning with what would be expected of separated flow [3]. As the slant angles became smaller, a clear low-pressure footprint formed around the upstream periphery of the slant. This low-pressure footprint aligned with the development of the streamwise-oriented vortices, drastically changing the pressure distribution, even though the geometry was only marginally different [3,36]. For the two minima in slant drag ($\alpha = 10^\circ$ and 35°), the slant with the higher angle indicated fully separated flow, while the other slant showed signs of the streamwise-oriented vortices just beginning to develop. This effectively produced a balance between reducing the low-pressure footprint from vortices and minimizing the surface normal on the opposing surface to reduce the streamwise component of pressure contributing to the drag.

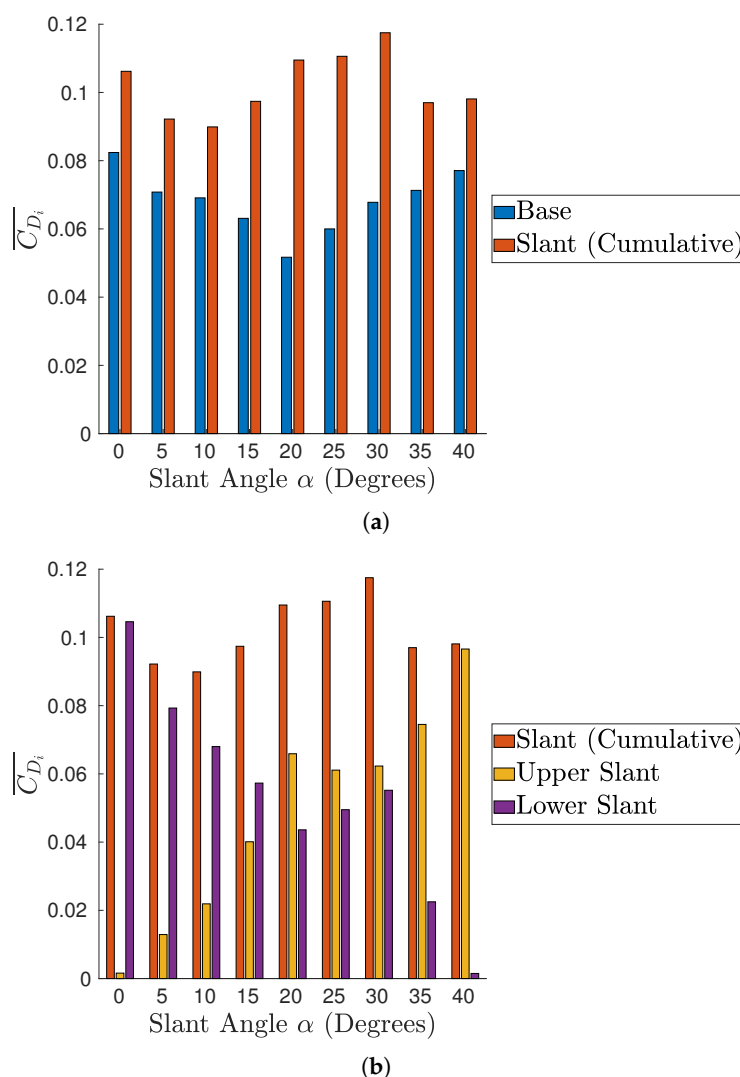


Figure 8. Breakdown of contributions to the total time-averaged drag of (a) base drag and slant drag, and (b) upper and lower slant drag $\overline{C_{D_i}}$ with respect to the upper slant angle α .

To connect the pressure footprint with the wake structures, we utilized the Ω -criterion [37] to identify the vortical structures in the wake (Figure 10). In general, the structure of the wake consisted of a torus near the base and a pair of streamwise-oriented vortices on the lower-angled slant. Exceptions to this included $\alpha = 25^\circ$, in which two pairs of streamwise-oriented vortices were produced (one by each slant), and two extreme angles ($\alpha = 0^\circ$ and 40°), in which no vortices formed and the torus became open. In nearly all cases, the asymmetry of the torus about the road-normal direction was evident. The orientation of the dominant (i.e., more bulged) side of the torus corresponded to the lower pressure formed on the base, as shown in Figure 9. Only the case where $\alpha = 25^\circ$ produced a nearly symmetric torus, again aligning with the base-pressure footprint. This shows that the base pressure correlated with the size and orientation of the torus formed past the base. Moving on to the streamwise-oriented vortices, there was a clear connection between the size of the vortices and the pressure footprint on each slant. As the vortices became larger, so did the low-pressure footprint. The drop in pressure was likely due to an increase in the strength of larger vortices, as Bulathsinghala et al. [6] previously demonstrated that the drag caused by the base slants is linearly proportional to the circulation of the slant vortices.

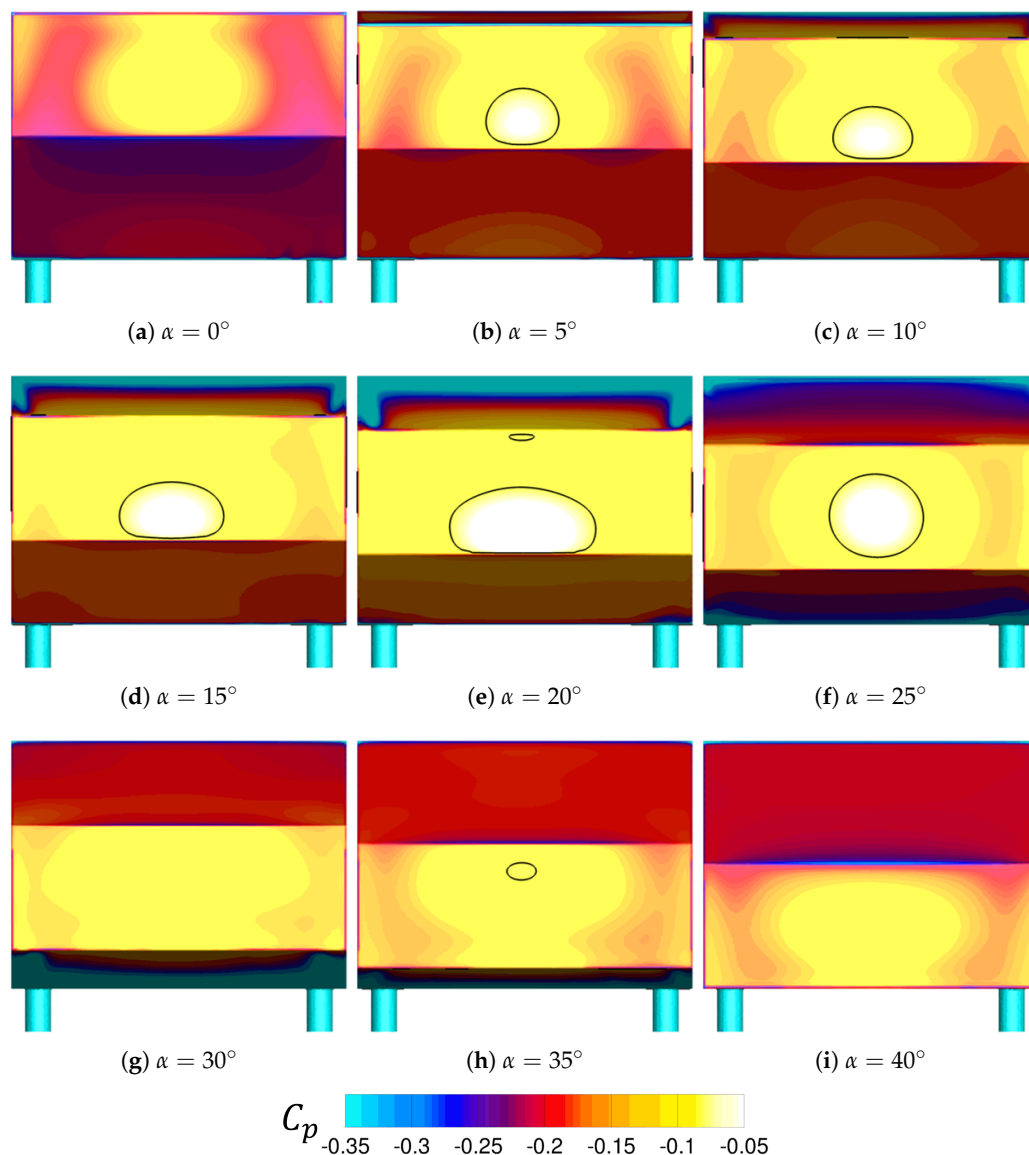


Figure 9. Time-averaged base pressure coefficient C_p with respect to the upper slant angle α . The solid black line highlights the contour line of $C_p = -0.09$.

To identify clear trends, we analyzed the torus and streamwise vortices in more detail. Starting with the torus, we used the streamline topology along the centerline ($y = 0$) to determine the location of the vortex centers via the foci [38,39] (Figure 11). At low angles of α , the upper vortex core was located much further downstream than the lower vortex core. As α increased, the upper vortex core moved closer to the base, decreasing the angle from the vertical and steadily moving closer to the lower vortex core until $\alpha = 20^\circ$. At downsweep angles greater than 20° , the vortex cores became nearly vertical. Instead, as the downsweep angles increased, the vortex cores were displaced, such that the center point between them was no longer centrally located on the base. Thus, the minimum in base drag corresponded to the vortex cores being nearly vertical and centrally aligned with the base, aligning with the concept of a symmetric wake for a bluff body torus [40].

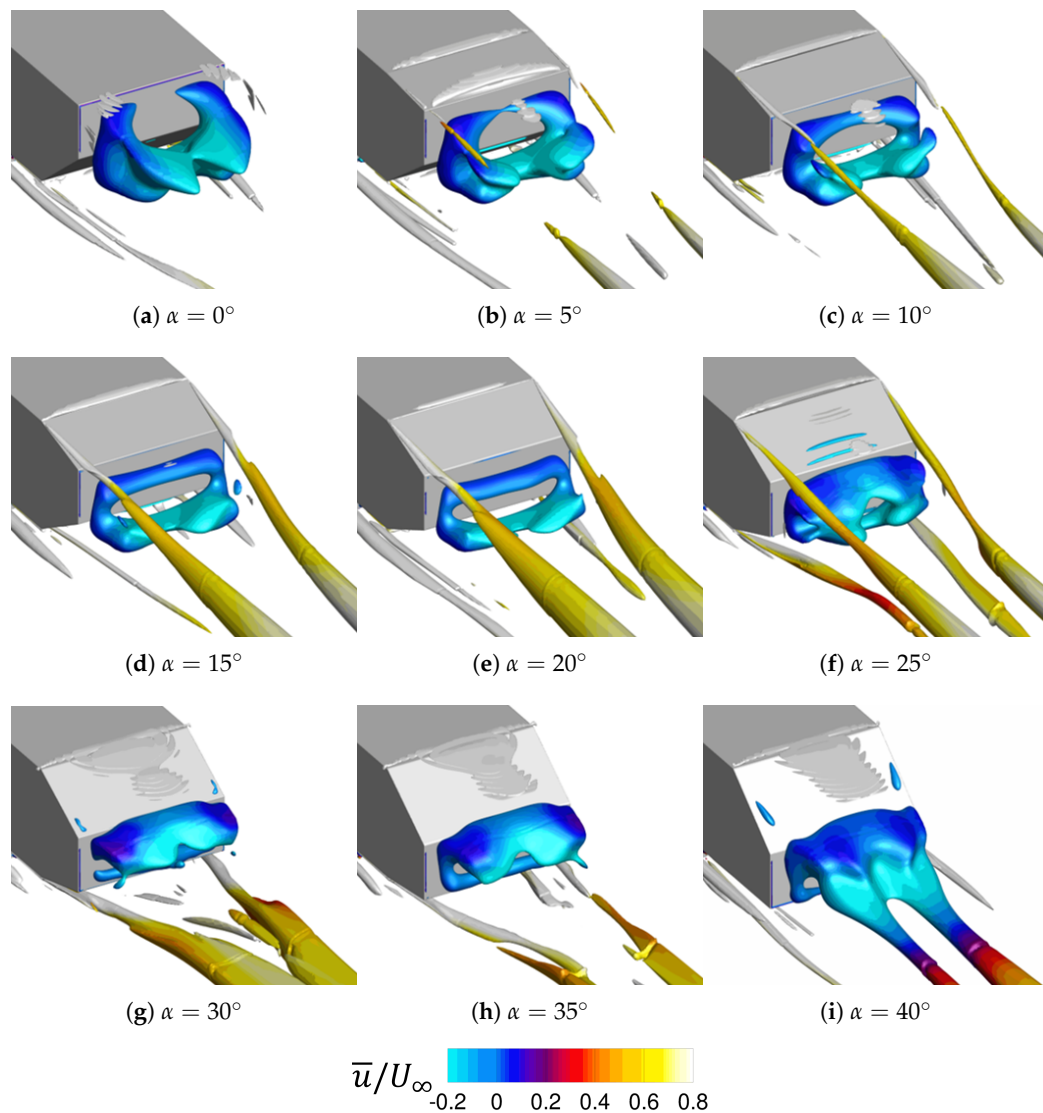


Figure 10. Time-averaged iso-surface of the Ω -criterion ($\Omega = 0.65$), colored by the time-averaged streamwise velocity \bar{u}/U_∞ .

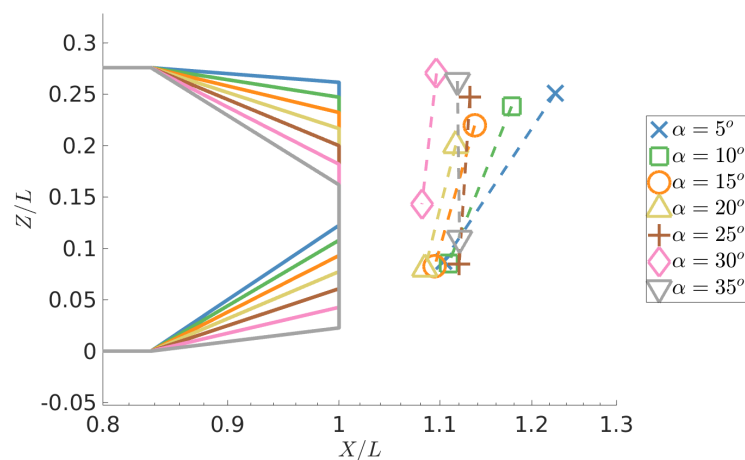


Figure 11. Time-averaged vortex core locations along the centerline ($y = 0$) with respect to the down-sweep angle α .

Next, we considered the slant vortices captured via the streamwise component of the time-averaged vorticity ω_x (Figure 12). At lower slant angles, there was a clear development

of streamwise-oriented vortices, as seen in the pressure footprints shown in Figure 9. As the slant angle increased, the vortices became larger, corresponding to the larger size of the lower-pressure footprint in Figure 9 and the increased slant drag shown in Figure 8b. However, the low-pressure footprint and subsequent slant drag decreased with increasing α or β values from $\alpha = 25^\circ$. Despite the vortices appearing at their largest size, as evidenced in Figure 10, they detached from the slant surface. This led to a reduction in the low-pressure footprint and the slant drag observed previously. Above $\alpha = 25^\circ$ or $\beta = 20.4^\circ$, the vortices were still present, but the size and concentration of the vorticity were greatly reduced compared to lower slant angles, even though this regime is typically described as fully separated [3,4]. Therefore, slant drag can be reduced by separating the vortices from the surface and/or reducing vortex strength.

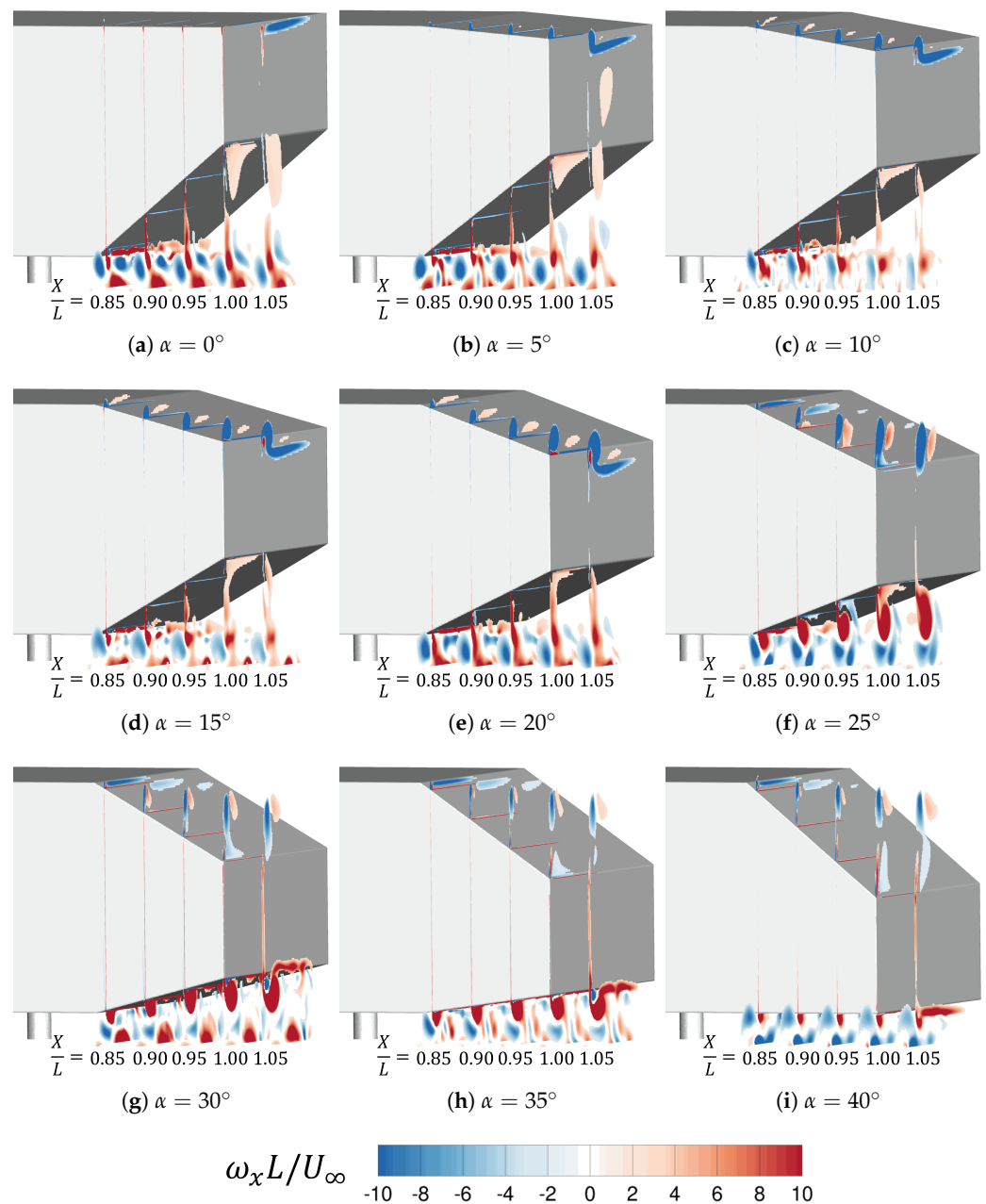


Figure 12. Streamwise normal slices of $y < 0$, colored by the contours of the time-averaged streamwise-oriented vorticity $\omega_x L / U_\infty$.

4. Conclusions

In this work, we used IDDES to simulate the flow around a double-slanted Ahmed body. We found that varying the slant angle while maintaining a constant base height resulted in a variation of 35 counts in vehicle drag. Although the drag produced by the slants was the predominant component, there was slightly greater variation in base drag than in slant drag. Drag on both the vertical base and slants was related to differing structures within the wake.

The vertical base was more directly affected by the structure of the wake torus. As the two slant angles became more equal, a higher stagnation pressure formed over a larger area of the base. The minimum base drag occurred when $\alpha = 20^\circ$ ($\beta = 25.4^\circ$). However, this was not the most symmetric wake, as is typically described for similar bluff body flows. Rather, this was the angle when the wake was nearly vertical (determined via the centerline foci) and nearly symmetric about the body in the road-normal direction.

The slant drag, on the other hand, was predominantly affected by the formation of a pair of streamwise vortices. While the vortices were always present, aside from the extreme angles that only produced a single slant, their state relative to the forming slant changed. At high angles, they separated from the corresponding slant, leading to a decrease in the pressure loss across the base. Although the pressure on the slant increased, greater slant angles resulted in an increased contribution of pressure to drag via the surface normal vector. At low angles, the vortices remained attached and increased in size and strength until separation as the slant angle increased. As long as the vortices were attached, there was a substantial increase in the low-pressure footprint on the slants. Thus, the two minima in slant drag ($\alpha = 10^\circ$ and 35°) occurred when one side produced separated vortices, while the other side had extremely weak vortices. To minimize drag, the base torus should be centrally aligned with the body, while the vortices should be reduced, eliminated, or separated from the slant surface.

Given the complexity of this flow, future work should focus on the relationship between the developing structures and the slant angle, as well as their correlation with pressure loss. In particular, the relationship between vortex strength and displacement from the vehicle surface with pressure loss is a complex and interesting problem. Additional work could be conducted through flow control to determine methods for either weakening and/or displacing the vortices from the body, as well as manipulating the orientation of the base torus.

Author Contributions: Conceptualization, M.A.; methodology, M.A.; validation, M.A.; formal analysis, M.A.; investigation, M.A.; resources, L.D.; data curation, M.A.; writing—original draft preparation, M.A.; writing—review and editing, L.D.; visualization, M.A.; supervision, L.D.; project administration L.D.; funding acquisition, L.D. All authors have read and agreed to the published version of the manuscript.

Funding: The current work was funded under the Strategic Partnership Agreement between The Ohio State University and Honda Development and Manufacturing of America LLC.

Informed Consent Statement: Not applicable.

Data Availability Statement: The original contributions presented in this study are included in the article. Further inquiries can be directed to the corresponding author(s).

Conflicts of Interest: The authors declare that this study received funding from Honda Development and Manufacturing LLC. The funder was not involved in the study design, collection, analysis, interpretation of data, the writing of this article, or the decision to submit it for publication.

Abbreviations

The following abbreviations are used in this manuscript:

CFD	Computational Fluid Dynamics
DES	Detached-Eddy Simulations
IDDES	Improved Delayed Detached-Eddy Simulations
LES	Large-Eddy Simulations
PISO	Pressure-Implicit with Splitting of Operators
RANS	Reynolds-Averaged Navier–Stokes
SIMPLE	Semi-Implicit Method for Pressure-Linked Equations

References

- Bonnaïon, G.; Cadot, O.; Évrard, A.; Herbert, V.; Parpais, S.; Vigneron, R.; Délery, J. On multistabilities of real car's wake. *J. Wind Eng. Ind. Aerodyn.* **2017**, *164*, 22–33. [[CrossRef](#)]
- Avadiar, T.; Thompson, M.; Sheridan, J.; Burton, D. Characterisation of the wake of the DrivAer estate vehicle. *J. Wind Eng. Ind. Aerodyn.* **2018**, *177*, 242–259. [[CrossRef](#)]
- Ahmed, S.R.; Ramm, G.; Faltin, G. Some salient features of the time-averaged ground vehicle wake. *SAE Trans.* **1984**, *93*, 473–503.
- Britcher, C.P.; Alcorn, C.W. Interference-free measurements of the subsonic aerodynamics of slanted-base ogive cylinders. *AIAA J.* **1991**, *29*, 520–525. [[CrossRef](#)]
- Morel, T. The effect of base slant on the flow pattern and drag of three-dimensional bodies with blunt ends. In *Aerodynamic Drag Mechanisms of Bluff Bodies and Road Vehicles*; Springer: Boston, MA, USA, 1978; pp. 191–226.
- Bulathsinghala, D.; Jackson, R.; Wang, Z.; Gursul, I. Afterbody vortices of axisymmetric cylinders with a slanted base. *Exp. Fluids* **2017**, *58*, 60. [[CrossRef](#)]
- Rossitto, G.; Sicot, C.; Ferrand, V.; Borée, J.; Harambat, F. Influence of afterbody rounding on the pressure distribution over a fastback vehicle. *Exp. Fluids* **2016**, *57*, 43. [[CrossRef](#)]
- Rossitto, G.; Sicot, C.; Ferrand, V.; Borée, J.; Harambat, F. Aerodynamic performances of rounded fastback vehicle. *Proc. Inst. Mech. Eng. Part D J. Automob. Eng.* **2017**, *231*, 1211–1221. [[CrossRef](#)]
- Cheng, S.Y.; Mansor, S. Rear-roof spoiler effect on the aerodynamic drag performance of a simplified hatchback model. *J. Phys. Conf. Ser.* **2017**, *822*, 012008. [[CrossRef](#)]
- Tian, J.; Zhang, Y.; Zhu, H.; Xiao, H. Aerodynamic drag reduction and flow control of Ahmed body with flaps. *Adv. Mech. Eng.* **2017**, *9*, 1687814017711390. [[CrossRef](#)]
- Siddiqui, N.A.; Agelin-Chaab, M. Investigation of the wake flow around the elliptical Ahmed body using detached Eddy simulation. *Int. J. Heat Fluid Flow* **2023**, *101*, 109125. [[CrossRef](#)]
- Tran, T.H.; Hijikuro, M.; Anyoji, M.; Uchida, T.; Nakashima, T.; Shimizu, K. Surface flow and aerodynamic drag of Ahmed body with deflectors. *Exp. Therm. Fluid Sci.* **2023**, *145*, 110887. [[CrossRef](#)]
- Maine, M.; El Oumami, M.; Bouksour, O. Aerodynamic Drag Reduction Around Vehicles Using a Curved Deflector. *Int. J. Integr. Eng.* **2023**, *15*, 24–36. [[CrossRef](#)]
- Kamacı, C.; Kaya, K. Numerical Investigation of Aerodynamic Properties of Ahmed Body for Different Rear Slanted Surface Configurations. *Eur. J. Sci. Technol.* **2021**, 469–475. [[CrossRef](#)]
- Krajnovic, S. 1020 Numerical Study of Drag Reduction of Generic Vehicle Body Using Impinging Devices. In Proceedings of the International Conference on Jets, Wakes and Separated Flows (ICJWSF), Nagoya, Japan, 17–21 September 2013; pp. 1020-1–1020-6.
- Viswanathan, H. Aerodynamic performance of several passive vortex generator configurations on an Ahmed body subjected to yaw angles. *J. Braz. Soc. Mech. Sci. Eng.* **2021**, *43*, 131. [[CrossRef](#)]
- Koppa Shivanna, N.; Ranjan, P.; Clement, S. The effect of rear cavity modifications on the drag and flow field topology of a square back Ahmed body. *Proc. Inst. Mech. Eng. Part D J. Automob. Eng.* **2021**, *235*, 1849–1863. [[CrossRef](#)]
- Huminic, A.; Huminic, G. Aerodynamic study of a generic car model with wheels and underbody diffuser. *Int. J. Automot. Technol.* **2017**, *18*, 397–404. [[CrossRef](#)]
- Huminic, A.; Huminic, G. Aerodynamics of curved underbody diffusers using CFD. *J. Wind Eng. Ind. Aerodyn.* **2020**, *205*, 104300. [[CrossRef](#)]
- Moghimi, P.; Rafee, R. Numerical and experimental investigations on aerodynamic behavior of the Ahmed body model with different diffuser angles. *J. Appl. Fluid Mech.* **2018**, *11*, 1101–1113. [[CrossRef](#)]
- Buscariolo, F.F.; Assi, G.R.; Sherwin, S.J. Computational study on an Ahmed Body equipped with simplified underbody diffuser. *J. Wind Eng. Ind. Aerodyn.* **2021**, *209*, 104411. [[CrossRef](#)]

22. Khalighi, B.; Chen, K.H.; Iaccarino, G. Unsteady aerodynamic flow investigation around a simplified square-back road vehicle with drag reduction devices. *J. Fluids Eng.* **2012**, *134*, 061101. [[CrossRef](#)]
23. Aljure, D.; Calafell, J.; Baez, A.; Oliva, A. Flow over a realistic car model: Wall modeled large eddy simulations assessment and unsteady effects. *J. Wind Eng. Ind. Aerodyn.* **2018**, *174*, 225–240. [[CrossRef](#)]
24. Hupertz, B.; Lewington, N.; Mockett, C.; Ashton, N.; Duan, L. *Towards a Standardized Assessment of Automotive Aerodynamic CFD Prediction Capability-AutoCFD 2: Ford DriveAer Test Case Summary*; Technical Report, SAE Technical Paper; SAE International: Warrendale, PA, USA, 2022.
25. Lienhart, H.; Becker, S. Flow and turbulence structure in the wake of a simplified car model. *SAE Trans.* **2003**, *112*, 785–796.
26. Shur, M.L.; Spalart, P.R.; Strelets, M.K.; Travin, A.K. A hybrid RANS-LES approach with delayed-DES and wall-modelled LES capabilities. *Int. J. Heat Fluid Flow* **2008**, *29*, 1638–1649. [[CrossRef](#)]
27. He, K.; Minelli, G.; Wang, J.; Gao, G.; Krajnović, S. Assessment of LES, IDDES and RANS approaches for prediction of wakes behind notchback road vehicles. *J. Wind Eng. Ind. Aerodyn.* **2021**, *217*, 104737. [[CrossRef](#)]
28. Aultman, M.; Disotell, K.; Duan, L.; Metka, M. Computational Modeling of Aerodynamic Design Trends for a Production SUV Subjected to Incremental Design Changes: Roof Spoiler and Underbody Geometry. *SAE Int. J. Passeng. Veh. Syst.* **2024**, *18*. [[CrossRef](#)]
29. Patankar, S.V.; Spalding, D.B. A calculation procedure for heat, mass and momentum transfer in three-dimensional parabolic flows. In *Numerical Prediction of Flow, Heat Transfer, Turbulence and Combustion*; Elsevier: New York, NY, USA, 1983; pp. 54–73.
30. Issa, R.I. Solution of the implicitly discretised fluid flow equations by operator-splitting. *J. Comput. Phys.* **1986**, *62*, 40–65. [[CrossRef](#)]
31. Aultman, M.; Wang, Z.; Duan, L. Effect of time-step size on flow around generic car models. *J. Wind Eng. Ind. Aerodyn.* **2021**, *219*, 104764. [[CrossRef](#)]
32. Lienhart, H.; Becker, S. 2003. Available online: https://www.kbwiki.ercofac.org/w/index.php?title=Test_Data_AC1-05 (accessed on 19 July 2024).
33. Ashton, N.; West, A.; Lardeau, S.; Revell, A. Assessment of RANS and DES methods for realistic automotive models. *Comput. Fluids* **2016**, *128*, 1–15. [[CrossRef](#)]
34. Graysmith, J.; Baxendale, A.; Howell, J.; Haynes, T. Comparisons between CFD and experimental results for the Ahmed reference model. In Proceedings of the RAeS Conference on Vehicle Aerodynamics, Loughborough, UK, 18–19 July 1994.
35. Strachan, R.; Knowles, K.; Lawson, N. The vortex structure behind an Ahmed reference model in the presence of a moving ground plane. *Exp. Fluids* **2007**, *42*, 659–669. [[CrossRef](#)]
36. Zigunov, F.; Sellappan, P.; Alvi, F. Reynolds number and slant angle effects on the flow over a slanted cylinder afterbody. *J. Fluid Mech.* **2020**, *893*, A11. [[CrossRef](#)]
37. Liu, C.; Wang, Y.; Yang, Y.; Duan, Z. New omega vortex identification method. *Sci. China Phys. Mech. Astron.* **2016**, *59*, 684711. [[CrossRef](#)]
38. Tobak, M.; Peake, D.J. *Topology of Three-Dimensional Separated Flows*; Technical Report; NASA: Moffett Field, CA, USA, 1981.
39. Perry, A.; Steiner, T. Large-scale vortex structures in turbulent wakes behind bluff bodies. Part 1. Vortex formation processes. *J. Fluid Mech.* **1987**, *174*, 233–270. [[CrossRef](#)]
40. Ahmed, D.; Morgans, A. Nonlinear feedback control of bimodality in the wake of a three-dimensional bluff body. *Phys. Rev. Fluids* **2022**, *7*, 084401. [[CrossRef](#)]

Disclaimer/Publisher’s Note: The statements, opinions and data contained in all publications are solely those of the individual author(s) and contributor(s) and not of MDPI and/or the editor(s). MDPI and/or the editor(s) disclaim responsibility for any injury to people or property resulting from any ideas, methods, instructions or products referred to in the content.